

Tartaric acid regulated the advanced synthesis of bismuth-based materials with tunable performance towards the electrocatalytic production of hydrogen peroxide

Paul Morandi,¹ Valerie Flaud,² Sophie Tingry,¹ David Cornu,¹ and Yaovi Holade^{1,*}

¹Institut Européen des Membranes, IEM UMR 5635, Univ Montpellier, ENSCM, CNRS, Montpellier, France.

²Institut Charles Gerhardt, ICGM UMR 5253, Univ Montpellier, ENSCM, CNRS, Montpellier, France

*Corresponding author: yaovi.holade@enscm.fr (Y.H.)

Abstract

Tartaric acid emerges as an ecofriendly organic for the biogenic preparation of micro- and nano-structured materials. For those synthesis mainly dictated by the coordination chemistry, questions remain open about the impact of the alkalinity on the nature of the resulting material as well as the properties. On the other hand, the design of advanced catalytic materials for the direct production of hydrogen peroxide from the air is particularly needed. We report herein new synthesis, physico-chemical and electrocatalytic insights from bismuth-based materials. It was found that the tight control of the alkalinity of the synthesis medium through the molar ratio $R = [\text{sodium hydroxide}]/[\text{bismuth (III) nitrate}]$ leads to the production of a library of bismuth-based materials composed of metallic, (oxy)hydroxide, and oxide structures owing to the bismuth-tartrate complexes as intermediates. Electroanalytical studies show an oxygen-to-hydrogen peroxide selectivity in 0.1 M KOH of 77, 88 and 92% for $R = 0, 12$ and 30 , respectively. In 1 M KOH, the selectivity is 90 and 96% for $R = 12$ and 30 , respectively. The production rate is 69 ± 3 and $44 \pm 3 \text{ mol kg}^{-1} \text{ cm}^{-2}$ during 2 h, corresponding to a faradaic efficiency of 92 ± 4 and $62 \pm 5\%$ for $R = 12$ and 30 , respectively. Those results place the present materials among the best known oxygen-to-hydrogen peroxide reduction catalysts without the need for preparing alloys or specific surface modification. This work contributes in engineering novel catalytic materials for the advanced application of the on-site production of valuable chemicals.

1. Introduction

Historically, the synthesis of diverse morphologies and sizes of micro- and/or nano-crystals for different biomedical and catalytic applications was guided by the use of a variety of organic molecules, prevalingly citric acid, polyvinylpyrrolidone (PVP), the cetyltrimethylammonium bromide (CTAB).^{1,2} The modification of the physico-chemistry of the reaction mixture results into chemical species acting as surfactants or capping agents. Furthermore, the tartaric acid was investigated as another natural carboxylic acid from plants to potentially substitute the citric acid in the preparation of colloidal metal nanoparticles,^{3,4} a field referred to as “biogenic synthesis” to face the growing need of environmentally compatible technologies in materials synthesis.^{3,5} The guiding principle behind the fabrication of colloidal particles when the tartaric acid is employed relies mainly on the coordination chemistry,⁶⁻⁸ which is triggered by the presence of many OH groups. This organic acid has been used to successfully prepare monodispersed nanoparticles of gold and silver for their optical properties deriving from the surface plasmon resonance.^{4,9} For their potential physico-chemical properties, bismuth-based materials such as Bi_2X_3 ($\text{X} = \text{S}, \text{Te}$, etc.) were also prepared in the presence of the tartaric acid.^{10,11} Belonging to the semimetal group, the small overlap between the bottom of the conduction band and the top of the valence band provides interesting physicochemical and catalytic properties to bismuth.¹²⁻¹⁵ For instance, bismuth-based composites gained a signification interest as active materials for the photo-/electrocatalytic synthesis of valuable chemicals (production of hydrogen peroxide,¹⁶ ammonia¹⁷, formate^{18,19}, hydrogen^{15,20,21}), the control of the catalytic selectivity,²²⁻²⁵ the sensing,²⁶ and energy conversion²⁷⁻³⁰ applications.

For the above end-uses, various synthesis methods were developed to prepared different types of micro- and nano-structured materials ranging from metallic Bi to Bi_2O_3 oxides depending on the designed synthesis protocol.^{8,18,19,27,29-31} Since tartaric acid is a triacid and bismuth salts are usually trivalent, the coordination chemistry in an aqueous medium for the production of a variety of morphologies and sizes is of particular interest to study, especially the effect of the alkalinity. Ma *et al.*⁸ reported the preparation of bismuth nanoparticles and their subsequent self-assembly into nanobelts, arguing that the formation of nanobelts depends on the amount of NaOH. Authors hypothesized that NaOH determines the reduction rates of the bismuth-tartrate complex

$[\text{Bi}_2(\text{C}_4\text{H}_2\text{O}_6)_2]^{2-}$, which influences the shape of the bismuth products.⁸ No in-deep physicochemical study was performed to correlate the composition of the produced materials to the reaction conditions. So, this study raised more questions about the role of alkalinity and especially the properties of materials that would result from such synthesis in the presence of tartaric acid since such organics can partially and even completely block the surface of the particles. A more comprehensive and focused study was therefore expected; in particular on how those materials would electrochemically react given the above applications of bismuth-based materials in electrosynthesis, and energy conversion/storage domains. For instance, photo- and electro-catalytic methods emerged in recent years as viable options to the high energy consumption anthraquinone process for the production of hydrogen peroxide, a chemical widely used in various industries.^{16,32-41} For electrocatalysts containing cost-effective non-noble metals, the alkaline medium is preferred to ensure chemical stability. Electrocatalytically, the two half-cell reactions and overall process describing the operation of an alkaline electrolyzer for the hydrogen peroxide production are resumed by Eqs. 1-3 since $\text{pKa}(\text{H}_2\text{O}_2/\text{HO}_2^-) = 11.75$. This would mean that a low cell voltage is required to drive electrocatalytically the hydrogen peroxide production if highly selective catalysts are found; hence their better design is expected.



Bi-based materials were found to be effective anode for the two-electron photocatalytic water-to- H_2O_2 process.^{16,42} However, to date, no electrocatalytic studies have been carried out on the potentiality of micro- and/or nano-structured bismuth materials derived from the above coordination chemistry with the tartaric acid. This would be worthwhile as the oxygen reduction reaction (ORR, Eq. 1) is highly sensitive to the surface state. Specifically, a high selectivity toward hydrogen peroxide is achieved when O_2 is perpendicularly adsorbed by a single atom on the catalytic surface, which is enabled by the inter-distance between active sites and the heterogeneity of the catalytic surface.⁴³⁻⁴⁵ It is therefore relevant to examine the potentiality towards ORR of the materials obtained by the coordination chemistry of tartaric acid. The direct hydrogen peroxide production from the oxygen is particularly important for the on-site treatment of organic pollutants

through the electro-Fenton process.⁴⁶⁻⁴⁹ To take up the above challenges, we aim in the present study to interrogate physico-chemically and electro-catalytically the effect of the molar ratio [sodium hydroxide]/[bismuth (III) nitrate] on the properties of the resulting bismuth-based materials. Specifically, we integrated various and complementary physical and electro-analytical techniques, namely the scanning electron microscopy (SEM), energy dispersive X-ray spectroscopy (EDX), X-ray photoelectron spectroscopy (XPS), thermogravimetric analysis (TGA), cyclic voltammetry (CV), linear sweep voltammetry (LSV), rotating ring-disk electrode (RRDE), electrochemical impedance spectroscopy (EIS), bulk electrolysis and UV-Vis assays. Our outcomes demonstrate that the different engineered types of bismuth-based micro- and nano-structured materials exhibit distinct surface and catalytic properties when the as-synthesized materials are employed in the specific application of electrochemical hydrogen peroxide production from oxygen.

2. Experimental Section

2.1. Chemicals and materials

Nitric acid (HNO₃, 65%, Sigma-Aldrich), potassium hydroxide (KOH, 99.98%, (trace metal basis), Acros Organics), bismuth (III) nitrate pentahydrate (Bi(NO₃)₂·5H₂O, 99.999%, trace metal basis, Sigma-Aldrich), isopropanol (iPrOH, ≥99.5%, Sigma-Aldrich), ethanol (96%, VWR), DL-tartaric acid (ReagentPlus[®], 99%, Sigma-Aldrich), sodium oleate (≥99%, Sigma Aldrich), sodium hypophosphite monohydrate (NaH₂PO₂·H₂O, ≥99%, Sigma-Aldrich), sodium hydroxide (NaOH, ≥98%, Sigma-Aldrich), Nafion[®] suspension (5 wt%, Sigma-Aldrich), potassium titanium (IV) oxide oxalate dehydrate (≥98% Ti basis, Sigma-Aldrich), sulfuric acid (98%, PanReac AppliChem ITW Reagents), potassium permanganate (≥99%, Sigma-Aldrich), hydrogen peroxide solution (30%, Sigma-Aldrich), filtration membrane (0.2 μm, Whatman) were used as received. Gas diffusion electrode (GDE, AvCarb MGL190, 190 μm thickness) was purchased from Fuel Cell Earth LLC (USA) and washed by iPrOH prior to use. The anion exchange membrane (Fumapem[®] FAA-3-50) was purchased from Fuel Cell Store (USA) and activated according to the procedure freely available on the internet website of the supplier. The water as solvent and used during the entire study was ultrapure and was obtained from a Milli-Q Millipore source (MQ, 18.2 MΩ cm at 20 °C).

2.2. Synthesis of different types of bismuth-based materials

The used procedure to synthesize bismuth-based materials was derived from a published method,⁸ but with some adjustments to be able to produce different types of materials. In a typical synthesis, a mass of 1.212 g of $\text{Bi}(\text{NO}_3)_3 \cdot 5\text{H}_2\text{O}$ was dissolved by stirring in 5 mL of an aqueous solution of 1.8 M HNO_3 ; all in a 500 mL three-neck round-bottom flask. Then, 0.6 g of tartaric acid and 15 mL of water were sequentially and slowly added, which results in the formation of a white suspension. Subsequently, a fixed volume of 35 mL of water containing NaOH, adjusted by the molar ratio $R = n(\text{NaOH})/n(\text{Bi}(\text{NO}_3)_3 \cdot 5\text{H}_2\text{O})$, was gently added under stirring. Ten types of materials were synthesized for ratios of 0, 2, 4, 6, 8, 12, 18, 24, 30 and 36. After the mixing, the reactor was transferred in a pre-heated oil-bath at 90 °C by resetting the vigorous agitation. After temperature stabilization, 0.015 g of sodium oleate was added. Next, 40 mL of 5 M sodium hypophosphite (reducing agent) were added at a flow rate of 8 mL min⁻¹ through a single channel infusion pump (KD Scientific) and the reaction was run for 5 h. Afterwards, the product was obtained from filtering on a Buchner system, washing successively with ethanol and water before drying in an oven at 40 °C overnight. The reactor was cleaned between two synthesis by procedure reported in ref.,⁵⁰ i.e., a combination of aqua regia (3 vol. of HNO_3 and 1 vol. HCl) and hot water.

2.3. Procedures of physicochemical characterizations

The morphology of the as-fabricated materials was analyzed by SEM on a Hitachi S-4800 microscope. The composition and homogeneity of the materials were studied by EDX, carried out on a ZEISS EVOHD-15 microscope. Crystallinity and phases identification were done by powder X-ray diffraction (PXRD), where the diffraction patterns were collected in Bragg-Brentano mode from 10 to 100° (in 2θ) using a PANalytical Xpert-PRO diffractometer operating at 40 kV and 20 mA ($\lambda(\text{CuK}\alpha_{1,2}) = 1.541 \text{ \AA}$). The analysis of the surface state and compositional were done by XPS on a Thermo Electron ESCALAB 250 spectrometer (15 kV, 6 mA) equipped with a monochromatic radiation source Al Mono ($\text{AlK}\alpha = 1486.6 \text{ eV}$). Survey spectra were recorded at 1 eV per step and 150 eV as pass energy. High-resolution spectra were obtained at 0.1 eV per step and 20 eV as pass energy. The AVANTAGE software was used for peaks fitting; the energy of C1s at 284.8 eV was used to correct/calibrate the binding energies. The quantification was done

by the routine XPS method. TGA was carried out on a SDT Q600 TA Instruments. About 5 mg of the material was put in an aluminum crucible and heated from the room temperature to 1000 °C at 5 °C min⁻¹ under air flow of 100 mL min⁻¹.

2.4. Procedures of electrochemical measurements

Cyclic voltammetry (CV) and bulk electrolysis experiments were performed on a SP-150 potentiostat (Biologic Science Instruments). ORR-RRDE analysis was carried out on an AUTOLAB PGSTAT128N bipotentiostat (Metrohm, Netherlands); including a Metrohm's RRDE setup of glassy carbon disk (0.196 cm²) and platinum ring (0.072 cm²). The potentiostatic electrochemical impedance spectroscopy (EIS) experiments were performed on an AUTOLAB PGSTAT204 potentiostat (Metrohm, Netherlands). Unless otherwise stated, all voltammograms have been post-corrected for ohmic drop, as determined by EIS. To prepare a homogeneous catalytic ink, 130 µL of water and 50 µL iPrOH were subjected to a vortex mixing followed by the addition of 5 mg of a desired material to undergo a sonication in a water bath. Before any catalytic ink deposition on the GC disk, RRDE was polished with alumina slurry of 3, 1 and 0.05 µm successively and washed with water before a final step of sonication in water for 5 min in order to remove any traces of remaining alumina. To get a good thin film of the catalytic ink onto GC, the RRDE was mounted on an inverted rotator shaft set at 0 rpm. After pipetting 4 µL onto the GC tip (loading of 0.5 mg_{cat} cm⁻²), the ink was subsequently dried under ambient conditions by increasing the rotator speed to 400 rpm and maintaining it until complete drying.^{51,52} The electrochemical measurements were performed on a home-made PTFE cell to withstand the alkalinity, operated at room temperature (22 ± 2 °C) and was frequently and rigorously cleaned by the permanganate method.⁵⁰ For CV experiments, the electrochemical measurements were recorded in a conventional three-electrode setup. The GC disk coated with the catalytic ink was the working electrode, a 12.4 cm² glassy carbon plate acted as the counter electrode and a mercury-mercury oxide electrode (Hg|HgO|KOH 0.1 or 1 M, MOE, RE-61AP Reference Electrode for alkaline solution, BAS Inc.) was used as the reference electrode. The potentials were then converted versus the reversible hydrogen electrode (RHE) according to the calibration relationship $E(\text{V vs RHE}) = E(\text{V vs MOE}) + \Delta E$. $\Delta E = 0.922 \text{ V}$ (0.1 M KOH) and 0.946 V (1 M KOH) at 25 °C in 0.1 and 1 M according to the calibrating curves shown in Fig. S1. Given the used electrolyte, a corrosion-resistant material was used for the solution outgassing and oxygen saturation, for instance the Tygon[®] XL-60 Clear,

Peristaltic Pump Tubing (Veber Caoutchouc, France). The accelerated stress test (AST) was performed by fast potential cycling from 0.3 to 0.9 V vs RHE at 100 mV s^{-1} in O_2 -saturated 1 M KOH for a total of 5000 cycles (1 cycle = forward and backward).

2.5. Procedures of electroanalytical measurements

Direct monitoring by the RRDE setup. The hydroxide peroxide in the form of HO_2^- in alkaline media ($\text{pK}_a(\text{H}_2\text{O}_2/\text{HO}_2^-) = 11.75$) and the overall exchanged number of electrons n_{exp} were determined online by Eqs. 4 and 5, respectively.^{50,53,54} For those RRDE measurements, a four-electrode potentiostat (also referred to as double- or bi-potentiostat) was utilized. RRDE was calibrated in N_2 -saturated 1 M $\text{KNO}_3 + 5 \text{ mM K}_3[\text{Fe}(\text{CN})_6]$ to determine its collection efficiency (N) defined as the fraction of the species formed at the disk that effectively arrives at the ring and reacts there, which was verified to be $24.5 \pm 0.5\%$ (Fig. S2), in agreement with the manufacturer's value of 24.9%.

$$\text{HO}_2^-(\%) = \frac{200}{1 + \frac{N|I_D|}{I_R}} \quad (\text{Eq. 4})$$

$$n_{\text{ex}} = \frac{4}{1 + \frac{I_R}{N|I_D|}} \quad (\text{Eq. 5})$$

I_D is the current from O_2 reduction at the disk and I_R is the current from the intermediate HO_2^- oxidation at the ring (note that current-potential curves were plotted according to IUPAC convention for which to a positive current is oxidation and a negative current is reduction⁵⁵).

Bulk electrolysis and UV-Vis assays. Bulk electrolysis was carried out in an H-type cell at room temperature ($22 \pm 2^\circ\text{C}$) for an applied potential of 0.6 V vs RHE (iR-uncorrected) and 2 h. The two compartments were separated by the anion exchange membrane. Anodic compartment contained 57 mL of outgassed 1 M KOH and a glassy carbon plate of 16.5 cm^2 as counter electrode. The cathodic compartment contained 57 mL of O_2 -saturated 1 M KOH, the reference electrode ($\text{Hg}|\text{HgO}|\text{KOH } 1 \text{ M}$) and the working electrode. The latter was made of a piece of GDE cut into a L-shape of 2 cm high and 1 cm wide (exposed area of 2 cm^2 , not taking into account its 3D structure) and enough space on the top for electrical wiring with gold. An aliquot of 41 μL of the

catalytic ink was gradually deposited onto each side and left to dry at room temperature to reach the same loading as RRDE, i.e., $0.5 \text{ mg}_{\text{cat}} \text{ cm}^{-2}$. The solution was gently stirred during electrolysis and O_2 flow (on surface) maintained. The samplings were firstly acidified toward pH 3.5, and the transformed H_2O_2 species ($\text{HO}_2^-_{(\text{aq})} + \text{H}^+_{(\text{aq})} = \text{H}_2\text{O}_2$, $\text{pK}_a = 11.75$) were secondly quantified by UV-Vis assays using potassium titanium (IV) oxalate as a colored indicator.^{40,56-58} For that, the absorbance of the yellow pertitanic acid complex between hydrogen peroxide and potassium titanium oxalate was measured at $\lambda = 390 \text{ nm}$ on a JASCO V-570 UV-Vis-NIR spectrophotometer. The faradaic efficiency (FE) also referred to as faradaic selectivity for the electrosynthesis of HO_2^- was evaluated from Eq. 6.

$$FE(\%) = \frac{\text{partial electricity used to produce } \text{HO}_2^-}{\text{total electricity}} \times 100 = \frac{n_{\text{exp}} C V F}{Q} \times 100 \quad (\text{Eq. 6})$$

$C(\text{mol L}^{-1})$ is the molar concentration of HO_2^- , $V(\text{L})$ is the volume of the electrolysis solution, $F(= 96485 \text{ C mol}^{-1})$ is the Faraday constant, $Q(\text{C})$ is the total electrical of charge passed through the reaction, and n_{exp} is the exchanged number of electrons ($n_{\text{exp}} = 2$ for $\text{O}_2\text{-to-HO}_2^-$).

3. Results and discussion

3.1. Preparation of various bismuth-based materials

The complexation between the tartaric acid and the bismuth (III) was used as a tool to design an advanced synthesis process that will allow us obtaining bismuth-based materials with different morphologies and subsequently modify their surface and structural properties. Scheme 1 resumes the designed methodology, which mainly relies on the change of the alkalinity of the reactor content that was adjusted by the sodium hydroxide base. Indeed, we first hypothesized that the change of the alkalinity in the starting colloidal solution should enable to regulate the complexation between the organic acid and the metallic cation. This would act as a basis to manipulate the seeding, growth and subsequent self-assembly into micro- and nano-structured materials. The latter will lay the foundation towards the preparation of composite and hybrid materials with advanced surface and electrocatalytic properties. Upon the addition of the tartaric acid to the reactor containing a dissolved bismuth (III) nitrate, a white temporary suspension attributed to the

$[\text{Bi}_2(\text{C}_4\text{H}_3\text{O}_6)_2]$ organic complex was rapidly formed.⁶⁻⁸ When sodium hydroxide was added, the previous white suspension disappeared for a certain amount (R higher than 12). This observation is explained by the deprotonation of the previous organic acid leading to a $[\text{Bi}_2(\text{C}_4\text{H}_2\text{O}_6)_2]^{2-}$ ion-complex,⁷ as highlighted in Scheme 1. By combining the acidity of the native tartaric acid ($\text{p}K_a = 3.0$ and 4.4) to the reduction kinetics of $[\text{Bi}_2(\text{C}_4\text{H}_3\text{O}_6)_2]$ and $[\text{Bi}_2(\text{C}_4\text{H}_2\text{O}_6)_2]^{2-}$ by the sodium hypophosphite, different types of bismuth products are expected. To rationalize our synthesis methodology, the amount of bismuth precursor was fixed and that of sodium hydroxide was changed according to the molar ratio $R = n(\text{NaOH})/n(\text{Bi}(\text{NO}_3)_3 \cdot 5\text{H}_2\text{O})$. This new design was highly motivated by the possibility to produce various bismuth materials ranging from metallic to oxide by a simple change of one parameter, which could inspire and facilitate further scaling up. We next carefully studied the produced materials by a set of physiochemical and electrochemical techniques before the evaluation of their ability towards the targeted electrocatalytic hydrogen peroxide production.

3.2. SEM and EDX analysis

We first utilized the microscopic techniques to determine whether the hypothesized production of different micro- and nano-structured bismuth-based materials by the change of the molar ratio $R = n(\text{NaOH})/n(\text{Bi}(\text{NO}_3)_3 \cdot 5\text{H}_2\text{O})$ was successful or not. Fig. 1 shows the SEM images at different magnifications for the materials obtained for $R = 0, 6, 12, 24$ and 30 . Additional SEM pictures are reported in Figs. S3-S9 to probe a wide spectrum of $R = 0$ to $R = 30$ and better see the effect of the alkalinity on the nature of the produced material. For $R = 0$ to $R = 6$, a brown color powder produced at a yield of about 100% (relative to the expected bismuth weight and the recovered one) and consisting of nano-scale particles of the order of 100 nm, which undergo a self-assembly process to yield micro-particles. As it can be observed in Fig. 1 and Figs. S3-S4, the materials produced at $R = 2-6$ are more homogeneous with a well-defined morphology than the material fabricated without any addition of NaOH ($R = 0$). For $R = 12$, a white solid was recovered with a yield of 142% and mainly composed of fibers of about 100 nm width and micro-sized in length (see Fig. 1 and Fig. S5). This extra yield and the color of the recovered product would indicate that a composite material was obtained, which may likely involve the hydration, hydroxyl or oxyhydroxyl-based system. Further complementary studies by EDX, XRD and XPS will provide more information. The material obtained at $R = 8$ (Fig. S3) is a transition between the metallic

state for $R = 0-6$ and the (oxy)hydroxyl one at $R = 12$. The ratio $R = 18$ was found to be another transition state towards the production of a black powder at a yield of 74%, which is mainly composed of microfibers and some microparticles (Fig. S6). Indeed, for $R = 24$, micro- and nano-scale particles materials were obtained at a chemical yield of 63% (Fig. 1 and Fig. S7). For $R = 30$ (Fig. 1 and Fig. S8), there is an overwhelming presence of micrometric particles of particular morphology (chemical yield of 60%) when we compared with the materials produced at $R = 0-6$. Increasing excessively the amount of NaOH up to $R = 36$ results in the obtaining of crystals of various shapes from spherical to rods (chemical yield of 32%) as evidenced in Fig. S9. The reason behind a yield below 100% is simply due to the filtration process in which smaller particles are unavoidably passing through the pores of the membrane. Those SEM characterizations highlight, for the first time, a strong discrepancy leading to three types of materials, $R = 0-6$, $R = 12$, and $R = 24-36$. Indeed, the only reported synthesis method⁸ did not result in the obtaining of the present materials. Those visual results confirm our postulated hypothesis and indicate that the growth and crystallization can be regulated by the modification of the alkalinity of the synthesis media. The detailed mechanism and driving force behind this synthesis will be discussed later in the manuscript when the materials will be well characterized. Furthermore, given the diverse morphologies and sizes of the as-synthesized materials, it is anticipated different trends in the electrocatalytic properties.

Having revealed and confirmed by SEM that we were able to prepare different composite and hybrid bismuth-based materials, we next sought to examine precisely the composition of those micro- and nano-structured materials. To address that, we utilized the EDX to focalize the study on the representative materials of $R = 0, 6, 12, 24$ and 30 . The results are presented in terms of the overall mass composition (Fig. 2a), the overall atomic composition (Fig. 2b), and the atomic ratio of oxygen/bismuth (Fig. 2c). The bismuth content was evaluated to be 95.6 ± 0.5 , 93.0 ± 2.1 , 75.0 ± 2.0 , 87.6 ± 2.0 , and $88.7 \pm 1.5\text{wt}\%$, for $R = 0, 6, 12, 24$ and 30 , respectively. Control analysis by TGA-DSC of the as-synthesized material at $R = 30$ confirmed the trend about the presence of water/carbon species of ca. 2 wt% (Fig. S10). The high atomic percentages in Fig. 2b are simply the result of the low molecular weight of oxygen and carbon compared to bismuth. If the presence of carbon could be attributed to the used complexing agent (tartaric acid) and stabilizer (sodium oleate), the disparity suggests that the remaining amount depends strongly of the type of materials.

The oxygen-to-bismuth atomic ratio given in Fig. 2c provides insightful information about the type of material that was formed. In all cases, the ratio is below 6, which allow us to rule out the simple crystallization of the $[\text{Bi}_2(\text{C}_4\text{H}_3\text{O}_6)_2]$ molecular complex or the $\text{Bi}_2(\text{C}_4\text{H}_2\text{O}_6)_2]^{2-}$ ion-complex (no sodium counter cation was detected by EDX) for which two atoms of bismuth correspond to 6 atoms of oxygen. Quantitatively, O/Bi atomic ratio is 0.17 ± 0.05 , 0.32 ± 0.09 , 2.55 ± 0.25 , 1.21 ± 0.3 , 1.18 ± 0.19 for $R = 0, 6, 12, 24$ and 30 , respectively. This would mean that three categories of materials were prepared. First, metallic state (Bi^0 , O/Bi = 0) was obtained for $R = 0-6$ where the observed oxygen results from the natural oxidation of bismuth when exposed to ambient air. Second, a hydroxide or oxyhydroxide state ($\text{Bi}(\text{OH})_3$ or BiOOH , O/Bi = 2-3) was obtained for $R = 12$. Third, an oxide state (Bi_2O_3 , O/Bi = 1.5) was obtained for $R = 30$ with substantial presence of metallic bismuth. Metallic and oxide materials are basically crystalline while the (oxy)hydroxide can exhibit an amorphous state. At this stage, it can thus be concluded that EDX has confirmed the observations made with the SEM. It consequently remains to confirm the crystallinity and phase identification by a more specialized technique, which is the purpose of the next section.

3.3. PXRD screening

The previous discussion of the SEM and EDX results has pointed out the possible synthesis of bismuth-based materials with different crystallinity and composition. To unambiguously verify those potentialities, we next performed the powder X-Ray diffraction (PXRD) for the entire ten materials that were prepared through the regulator $R = n(\text{NaOH})/n(\text{Bi}(\text{NO}_3)_3 \cdot 5\text{H}_2\text{O})$. Fig. 3 displays the obtained PXRD patterns of the as-synthesized bismuth-based materials at different molar ratio. The measurements were made under the same experimental conditions. From the Fig. 3a, the overall comparison of the ten types of materials for $R = 0-36$ already reveals a difference in intensity and the number of peaks. A separation (Fig. 3b, $R = 6-36$) and indexed patterns (Figs. 3b-c, $R = 8-36$ and $R = 0-6$) allow examining closely the different situations. For $R = 0-8$, the diffraction peaks at $27.2, 38.0, 39.8, 44.7, 46.1, 48.9, 56.2, 62.3, 64.7^\circ$, correspond to (012), (104), (110), (015), (113), (202), (024), (116), and (122) reflections of rhombohedral bismuth (metallic), respectively.^{8,59-61} The observed peaks at 22.5 and 23.8° in Fig. 3a are assigned to the (003) and (101) reflections of that metallic bismuth.^{8,60,61} This bulk diffraction characterization clearly demonstrates that metallic micro-structured particles of bismuth are obtained when R is below 12,

which is in full agreement with the previous EDX analysis where the O/Bi atomic ratio of 0.17 ± 0.05 suggested the presence of oxygen at metallic bismuth by a natural surface oxidation. Besides, a deeper look at the PXRD patterns of the samples obtained for $R = 12$ and $R = 18$ suggest that those materials are amorphous, which may be likely $\text{Bi}(\text{OH})_3$ or BiOOH and support again the EDX results. However, when R was further increased up to 36, diffraction peaks were observed in addition to those of metallic bismuth. Specifically, the diffraction peaks observed at $24.9, 27.8, 30.5, 33.1, 41.8, 49.2, 52.6$, and 54.2° were indexed to the tetragonal structure of Bi_2O_3 with (210), (201), (211), (220), (212), (410), (411), (203) planes, respectively.^{8,27-29} This set of results by PXRD fully supports the successful design of a synthesis methodology to engineer different types of micro- and nano-structured bismuth-based materials with different shape, composition and crystallinity. Those characteristics will undoubtedly be a powerful tool to control the electrocatalytic selectivity towards the oxygen reduction to hydrogen peroxide. Considering that the targeted application for these materials in the present work concerns surface reactions, it is also important to examine their surface state in a sufficient detail. This will be the scope of the forthcoming section.

3.4. XPS probing

The preceding outcomes by SEM, EDX, and PXRD demonstrated that the regulation of the synthesis by the molar ratio $R = n(\text{NaOH})/n(\text{Bi}(\text{NO}_3)_3 \cdot 5\text{H}_2\text{O})$ has enabled the development of three classes of bismuth-based materials. Given the sensitivity of bismuth to natural oxidation and the targeted application in heterogeneous catalysis, we further used XPS to probe the surface state and composition more closely. Figs. 4a-e show the high-resolution spectra of the Bi 4f region for the different type of materials. The presence of metallic bismuth at an oxidation state zero (Bi^0) through the electrons of the Bi-Bi bond has been assigned to the binding energy of the Bi $4f_{7/2}$ between 157.2 and 158.1 eV.⁶²⁻⁶⁶ Herein, we observed a peak with a much lower binding energy of Bi $4f_{7/2} = 156.5$ eV. Similar observation was made in literature and assigned to the metallic bismuth involved in organic molecules with Bi-O- bonds,⁶³ here resulting from the remaining trace of organics that were used as complexing agent or stabilizer. The presence of $\text{Bi}(\text{OH})_3$ with Bi-OH bonds either coming from the spontaneous surface oxidation or the direct synthesis was evidenced by the component with a peak at Bi $4f_{7/2} = 158.4 \pm 0.4$ eV.^{62,64} The peak with the binding energy at Bi $4f_{7/2} = 158.8 \pm 0.3$ eV corresponds to the O=Bi-OH bonds in the oxyhydroxide

BiOOH.^{62,64} Finally, the Bi₂O₃ phase with Bi-O-Bi bonds was suggested for the peak a binding energy of Bi 4f_{7/2} at 161.0 ± 0.4 eV even if it normally appears around 160.3 eV.⁶²⁻⁶⁴ This proposition was mainly supported by the fact that in EDX (Fig. 2c), O/Bi is much more closed to Bi₂O₃ species, which also appears in XRD patterns only when $R \geq 24$ (Fig. 3). Furthermore, the quantitative data shown in Fig. 4f indicate that the surface is mainly composed of Bi(OH)₃ for the entire materials, which results from the natural oxidation of bismuth and hides the trends observed by both PXRD and EDX. It can, however, be observed that more Bi⁰ species are present at the surface for R below 12 while the amount of Bi₂O₃ species augments for R larger than 12. Fig. 5a illustrates the portion of the material that is typically analyzed by XPS with a depth of 1-5 nm, which can explained why Bi(OH)₃ was predominantly observed in Fig. 4. Fig. 5b gives an overall surface atomic composition of the chemical species as-quantified from XPS, which are oxygen, carbon and bismuth. The trend is not the same in comparison to the results obtained by the EDX in Fig. 2, which is explained by the analyzed depth by both techniques. The high amount of carbon species is explained by the remaining trace of organics that could be easily eliminated by the electrochemical treatment with cyclic voltammetry, which is efficient in removing organic molecules without perturbing the shape or morphology of the particles.⁶⁷⁻⁶⁹ The next section will aim to provide the electrochemical characteristics of those well-characterized materials by SEM, EDX, TGA-DSC, XRD, and XPS.

3.5. Electrochemical analysis

In a further attempt to simultaneously determine the electrochemical characteristics of the as-fabricated materials while evaluating their catalytic performance towards the ORR, we next utilized the CV in 0.1 M KOH. To bring out a comprehensive understanding, we considered the four classes of materials obtained at $R = 6, 12, 24$ and 30 with a comparison to the control sample obtained for $R = 0$. The blank CVs at 100 mV s⁻¹ were recorded in the outgassed electrolyte while those for ORR were obtained after saturation with O₂. Figs 6a-e and Figs. S11-S14 show the obtained CVs. It should be pointed out that stable CVs were obtained after 30 cycles, which is common in electrochemistry to stabilize the surface. This also aims to potentially remove any remaining organic compounds as it was mentioned in the previous paragraph. Typical profiles of the successive CVs recorded at 100 mV s⁻¹ in Ar-saturated 0.1 M KOH were reported Fig. S11. The blank CV profile is different from one electrode to another one, which supports the idea of the

preparation of different types of materials. During the positive scan, the anodic peaks were attributed to the oxidation of bismuth (0) to bismuth (III) to form BiOOH, Bi(OH)₃, and Bi₂O₃ species.^{27-30,70-72} It was reported that the pre-peak corresponds to a small fraction of Bi metal sites located near the bismuth-metal/micropore-solution interface while the main and the plateau are related to the oxidation of bismuth metal to bismuth (III).⁷⁰ During the reverse scan, the main cathodic peak corresponds to the reduction of the previously formed bismuth (III) to bismuth metal, which is considered to be composed of several steps and where the intermediate species BiO₂²⁻ was used to explain the presence of at least one cathodic peak.^{70,73} The effects of the upper potential (Fig. 6f and Fig. S13) and the scan rate (Fig. S14) confirm the excellent reversibility of the oxidation and reduction processes observed in Figs. 6a-e. The present bismuth-based materials have a lower peak-to-peak gap in comparison to other reported bismuth materials.^{27-30,71,74-77} This high capacity of reversibility could therefore give rise to further application in electrochemical super-capacitor for the energy production and storage with an outstanding performance.^{27-30,71,74-77} The evaluation of the charging-discharging is beyond the scope of the present work.

In the presence of O₂, the first cycle shows the appearance of a reduction wave starting at about 0.9 V vs RHE. As it is reported in Fig. S12, the reduction peak returns to its normal profile and position after the 2nd cycle. The presence of the pre-peak for the electrode fabricated from the material $R = 12$ suggests that the electrocatalytic oxygen reduction reaction had induced a restructuring of the surface of the material or provided a better surface cleaning. Indeed, carbon monoxide oxidation at metallic surfaces had been employed as an electrochemical cleaning method when the synthesis method involved the use of organic molecules.⁷⁸ Overall, those preliminary tests by CV performed in the presence of O₂ already suggest a good activity towards the electrocatalytic oxygen reduction reaction. It now remains to evaluate the depth of the reduction of this oxygen to know if it is a complete phenomenon with four transferred electrons ($O_2 + 2H_2O + 4e^- \rightarrow 4HO^-$) or partially two electrons to produce hydrogen peroxide ($O_2 + H_2O + 2e^- \rightarrow HO_2^- + HO^-$) as targeted herein.

3.6. Sketch of the developed synthesis process for various types of bismuth-based materials

The entire experimental results obtained from the physicochemical and electrochemical techniques were combined to make a scheme illustrating the different scenarios. Scheme 2 shows the proposed different steps. The step (a) is the dissolution of the $\text{Bi}(\text{NO}_3)_3 \cdot 5\text{H}_2\text{O}$ precursor in the nitric acid solution in order to avoid precipitation in the hydroxide form. Seminal work showed that when sodium tartrate is added to an acetic acid solution containing bismuth nitrate, a white precipitate is formed, which contains 58.3% of bismuth, closed to the $[\text{Bi}_2(\text{C}_4\text{H}_3\text{O}_6)_2]$ compound (indicated in the step (b)).⁷ This situation is therefore slightly similar to the material obtained in the case of $R = 12$ in which some traces of the complex may exist. It should be underscored that we unambiguously demonstrated by different set of techniques that it is not exactly the situation and the previous authors did not performed any reduction as we run herein. Furthermore, the extra amount of sodium hydroxide that was needed to dissolve this white suspension and form $[\text{Bi}_2(\text{C}_4\text{H}_2\text{O}_6)_2]^{2-}$ is explained by the initial acidity of the solution and the requirement to deprotonate the native tartaric acid ($\text{pK}_a = 3.0$ and 4.4) before complexation. Depending on the amount of the sodium hydroxide, either the $[\text{Bi}_2(\text{C}_4\text{H}_3\text{O}_6)_2]$ molecular complex or the $[\text{Bi}_2(\text{C}_4\text{H}_2\text{O}_6)_2]^{2-}$ carboxylate is further reduced by the sodium hypophosphite to synthesize bismuth particles and release the tartrate as by-product. The step (c) accounts another situation, whereby the bimolecular complex undergoes a partial or full hydrolysis in the presence of a high amount of sodium hydroxide to generate different types of bismuthyl bismuth sodium tartrate.⁷ Given the initial acidity of the medium and the findings from different characterizations, we conclusively hypothesized that: (i) the materials obtained for $R = 0-6$ correspond to the bismuth precursor described by Scheme 2a, (ii) the material obtained for $R = 12$ is better described by the bismuth precursors presented in Scheme 2b, and (iii) the materials obtained for $R = 18-36$ likely originate from the bismuth precursors drawn in Scheme 2c.

3.7. Catalytic performance towards electrochemical hydrogen peroxide production

We finally combined different electroanalytical methods to evaluate the electrocatalytic performance of the as-synthesized materials. The first setup was the rotating ring-disk electrode (RRDE), described by Eqs. 4, and 5. Fig. 7 shows the obtained results in 0.1 M KOH electrolyte for the different and representative materials obtained at $R = 0, 6, 12, 24$, and 36 . The blank experiments were performed when no catalytic ink was deposited and referred to as GC (glassy carbon). We initially recorded the open circuit potential (OCP), which is a thermodynamic

indicator of the reaction feasibility. OCP stabilizes to 0.93, 0.93, 0.85, 0.80, and 0.85 V vs RHE for $R = 0, 6, 12, 24,$ and 36 , respectively (0.85 V vs RHE for GC). Those values are slightly larger than the expected potential of the process $\text{O}_2 + \text{H}_2\text{O} + 2\text{e}^- \rightarrow \text{HO}_2^- + \text{HO}^-$, $E^\circ = 0.76$ V vs RHE. This could thus suggest that the starting process is $\text{O}_2 + 2\text{H}_2\text{O} + 4\text{e}^- \rightarrow 4\text{HO}^-$ for which $E^\circ = 1.23$ V vs RHE. It should however keep in mind that OCP is not a fair descriptor since unlike H_2 oxidation, the oxygen reduction has low kinetic so that the onset potential does not always match with the OCP. So, we further recorded the LSV curves to simultaneously visualize the disk current density coming from the oxygen-to-hydrogen peroxide reduction process and the ring current density resulting from the oxidation of the produced hydrogen peroxide. Fig. 7b displays the obtained LSV where the onset potential was found to be 0.75 ± 0.05 V vs RHE, thus in line with a two-electron transferred process (Eq. 1). The quantitative results in Fig. 7c show that, at 0.6 V vs RHE, the couple of data associated to the hydrogen peroxide selectivity and real overall transferred number of electrons ($\%\text{HO}_2^-$, n_{ex}) for the different investigated materials is GC (88%, 2.2e-), R0(84%, 2.3e-), R6(63%, 2.7e-), R12(83%, 2.3e-), R24(53%, 2.9e-), R30(88%, 2.2e-). At 0.5 V vs RHE, the performance is GC(88%, 2.2e-), R0(77%, 2.5e-), R6(63%, 2.7e-), R12(88%, 2.2e-), R24(59%, 2.8e-), R30(92%, 2.1e-). It can clearly be observed that the material $R = 0$ is gradually losing its efficiency while $R = 12$ and $R = 30$ maintain a good performance in hydrogen production. Even if GC showed a competitive selectivity, it should be pointed out that it has no real interest given its very high cost and the low current density obtained in the potential range of 0.4-0.6 V vs RHE, which are expected for the implementation in practical electrolyzers. By taking the disk current density at ca. 0.45 V vs RHE as the limiting current density, the mass-corrected kinetic current density normalized to the amount of the catalyst (j_k) was determined to compare the different catalysts. The results are plotted as Tafel plots in Fig. 7d. At 0.55 V vs RHE, $j_k = 3.4, 8.8, 44.9, 3.7,$ and 9.7 A g^{-1} for $R = 0, 6, 12, 24,$ and 30 , respectively. Those results of selectivity and kinetic current density show that the materials obtained for $R = 12$ and $R = 30$ are the best performing catalysts.

The values of the Tafel slope, which is a mechanism and kinetic descriptor, support the previous choice. Before comparing our results to the existing literature with other types of electrocatalysts (no bismuth-based materials have been reported to date),^{33-35,39,79-82} we also utilized electrochemical impedance spectroscopy (EIS) for modeling the electrocatalytic interface as well as confirming the trends observed for the Tafel slope. The results in terms of the complex-plane

Nyquist impedance at 0.67 V vs RHE are shown in Fig. 7e with inset the corresponding electrochemical equivalent circuit of $R_{\Omega} + Q_{CPE} // R_{ct}$, where R_{Ω} is the ohmic resistance, Q_{CPE} is the capacitance of the constant phase element and R_{ct} is the charge transfer resistance (proportional to the rate constant).^{83,84} The extracted data are reported in Table S1 and the charge transfer resistance was used to draw the Tafel plots shown in Fig. 7f. The lowest charge transfer resistance was observed for $R = 12$ and $R = 24$, which was expected given the LSV profiles in Fig. 7b. Taking into account the selectivity for the targeted application, we concluded that $R = 12$ and $R = 30$ should be prioritized for further deep investigation. All the above results highlight that the best selectivity towards the electrochemical hydrogen peroxide production is achieved when the starting materials contain oxygen species. The heterogeneous surface composed of bismuth and oxygen atoms consequently favors the perpendicular adsorption of the molecular oxygen.^{43,44,85} To achieve this perpendicular adsorption of O_2 by a single atom on the catalytic surface, the driving force is the spacing between adjacent active sites and the heterogeneity of the catalytic surface that modulates the electronic interactions. This explains the low performance of the metallic material in comparison to the oxides and the oxy-hydroxides materials. The results obtained in 1 M KOH electrolyte are shown in Fig. 8 and Fig. S15 at the different speeds of the RRDE. The slight fluctuation in Figs. 8b, d, f with the rotating speed is normal and is simply because the collection efficiency itself undergoes fluctuations (see Fig. S2a). The quantitative data gathered in Table 1 demonstrate that a better efficiency is obtained with the material $R = 30$ (95.5%, $2.1e^-$, and 30 A g^{-1} at 0.6 V vs RHE for 1600 rpm) in comparison to the material R12 (90.2%, $2.2e^-$, and 29 A g^{-1} at 0.6 V vs RHE for 1600 rpm). Since long-term stability matters for a practical application, we performed an accelerated stress test (AST) for the catalyst that gives the best performance ($R = 30$). This was carried out in O_2 -saturated 1 M KOH and was composed of 5000 cycles of CV in the potential window where the material is electrocatalytically active, i.e., 0.3-0.9 V vs RHE. The results in Fig. 8e,f, Table 1 and Fig. S15 clearly demonstrate that the catalytic material exhibits an outstanding stability and performance with a slight improvement of the mass-corrected kinetic current density after this accelerated ageing program (95% , $2.1e^-$, and 68 A g^{-1} at 0.6 V vs RHE for 1600 rpm). For the comparison with the recent and existing data, the obtained high kinetic current density, at 0.55 V vs RHE, of 977, 929, and 965 A g^{-1} for R12, R30 and R30-AST, respectively, outperform the reported values of 73-600 A g^{-1} .^{34,79,80,82}

To confirm the efficiency observed with the RRDE method, hydrogen peroxide was spectrophotometrically tracked following bulk electrolysis, which was done with the catalyst deriving from $R = 30$. To this end, 2 hours electrolysis at an applied potential of 0.6 V vs RHE (iR-uncorrected) was carried out in an H-type cell, wherein the two compartments were separated with an anion-exchange membrane. The entire results are shown in Fig. 9. Before the bulk electrolysis, control CVs were taken at 100 mV s^{-1} in the H-type cell for the bare carbon paper (CP) electrode and the ink-modified CP electrode (CP-R30). Fig. 9a shows the CV profiles in the absence and presence of oxygen, which are similar to the findings of Fig. 6 (note that the three dimensional (3D) structure of the carbon paper can slightly alters the voltammogram). This result justifies the choice of 0.6 V vs RHE for the electrolysis. Furthermore, the bare carbon paper has activity towards the electrocatalytic oxygen reduction at the applied potential of 0.6 V vs RHE. This explains the high value of the recorded electrical charge that was passed during the potentiostatic electrolysis. Fig. 9c depicts the UV-Vis spectra of a sulfuric acid + potassium titanium oxalate solution in the absence and presence of the hydrogen peroxide resulting from the electrolysis (after stabilization to pH = 3.5). This control experiment confirms that the wavelength of $\lambda = 390 \text{ nm}$ resulting from the pertitanic acid complex between and potassium titanium oxalate can be utilized to selectively quantify any produced hydrogen peroxide as previously reported.^{40,56-58} Fig. 9d and Table 1s report the quantified hydrogen peroxide by the UV-Vis assays by two metrics. Those findings in terms of the produced hydrogen peroxide and faradaic efficiency (FE, %) after 2 hours of electrolysis are: (i) $69 \pm 3 \text{ mol kg}^{-1} \text{ cm}^{-2}$ and $92 \pm 4 \%$ for CP-R30, (ii) $44 \pm 3 \text{ mol kg}^{-1} \text{ cm}^{-2}$ and $62 \pm 5\%$ for CP-R12, and (iii) $38 \pm 4 \text{ mol kg}^{-1} \text{ cm}^{-2}$ and $37 \pm 3\%$ for CP. Those quantitative analytical results support the high performance for the catalyst fabricated from the materials obtained by $R = 30$. The production rate are comparable to up-to-date data gathered in ref.³⁴ In additional to that, it is important to mention that the faradaic yield of $92 \pm 4\%$ is higher than the reported efficiency of 70-87%^{39,79} and approaches the benchmarked record values of 94-95%.^{33,35}

We finally performed post-mortem SEM and HRSEM of the CP-R30 electrode after the bulk electrolysis to reveal the localization and morphology of the particles within the 3D network of the carbon paper support. Figs. 9e,f present the recorded pictures, taken at different places. It can be seen that the particles are well attached to the surface of the microfibers as it is indicated in Fig. 9f. However, a slight modification of the morphology is observed in the high-resolution image, which could be attributed to the electrochemical treatments consisting of preliminary thirty cyclic

voltammograms recorded in argon-saturated electrolyte and the coulometry experiment in the presence of oxygen. Fig. 9d demonstrates that the activity was maintained since the electrical charge is increasing. Furthermore, it can be also observed that the catalytic particles did not cover the entire surface of the microfibers within the 3D network of the carbon paper. Those observations rationally explain the slight decrease in faradaic efficiency that was observed during the bulk electrolysis experiment when compared to the value obtained by the RRDE method. This was expected since the carbon paper has a lower selectivity (Fig. 9d). Indeed, as it is impossible to cover all the microfibers of the carbon paper with the catalytic ink because of the 3D structure, a part of the input electricity will be used to drive O₂ reduction at the carbon paper. In the case of the RRDE, a thin film has been obtained so that the observed activity can be entirely attributed to the bismuth material.

4. Conclusion

We presented in this contribution a work dealing with the preparation and characterization of advanced bismuth-based materials designed by the coordination chemistry and for the specific application of the direct electrosynthesis of hydrogen peroxide from oxygen. The successful preparation of different types of those catalytic materials was based on a strict control of a single experimental parameter, namely the molar ratio $R = n(\text{NaOH})/n(\text{Bi}(\text{NO}_3)_3 \cdot 5\text{H}_2\text{O})$, which was varied from 0 to 36. The alkalinity and the tartaric acid as an eco-friendly organic molecule were combined together to regulate the formation of bismuth-based organic complexes as the initial building blocks. The latter further grow to yield bismuth particles with tunable properties and catalytic efficiency. From a set of physiochemical (SEM, EDX, XRD, and XPS) and electrochemical (CV) methods, the findings indicate that three classes of materials can be easily and conveniently produced depending on the value of the regulator R . Specifically, metallic bismuth (Bi), bismuth (oxy)hydroxide (BiOOH/Bi(OH)₃), and bismuth oxide (Bi₂O₃) were obtained for $R = 0-8$, $R = 12$, and $R = 24-36$, respectively. These materials were applied to the electrosynthesis of hydrogen peroxide, which was qualitatively and quantitatively studied by the rotating ring-disk electrode (RRDE), electrochemical impedance spectroscopy (EIS), bulk electrolysis and UV-Vis. It was observed that the co-existence of both bismuth and oxygen atoms in the catalytic material is critical for targeting high selectivity. Specifically, at 0.5 V vs RHE in

0.1 M KOH, the selectivity towards hydrogen peroxide production was 63% for $R = 6$ (metallic bismuth) while high values of 88 and 92% were achieved when $R = 12$ (bismuth (oxy)hydroxide) and $R = 30$ (bismuth oxide), respectively. A high kinetic current density was also recorded in 1 M KOH (0.55 V vs RHE, 1600 rpm), 977 A g⁻¹ (selectivity of 90%) for $R = 12$, and 929 A g⁻¹ (selectivity of 96%) for $R = 30$, which are significantly higher than the reported values of 73-600 A g⁻¹. The performed accelerated ageing program of 5000 voltammetry cycles highlights the outstanding stability and performance of the material obtained at $R = 30$ with a selectivity of 95% and a mass current density of 965 A g⁻¹. After integrating those materials in practical anion exchange membrane electrolysis cell, the material at $R = 30$ maintains high faradaic yield of 92 ± 4% with hydrogen peroxide productivity of 69 ± 3 mol kg⁻¹ cm⁻² over a 2 hours period. The findings of 62 ± 5% in faradaic efficiency and 44 ± 3 mol kg⁻¹ cm⁻² productivity for the material at $R = 12$, definitely underpins the importance of Bi₂O₃ phase on the high performance. The achieved faradaic efficiency of 92 ± 4% is larger than the reported 70-87% and approaches the record values of 94-95%, which opens news opportunities for the future deployment of the present materials in electrochemical systems.

Supplementary Information

† Electronic supplementary information (ESI) available.

Conflicts of interest

The authors declare no competing financial interest.

Acknowledgment

This work was funded by the European Institute of Membranes of Montpellier through the Exploratory Project COGENFC (PAT-Axis-Energy-2018). We thank Didier Cot, Bertrand Rebiere, and Arie van der Lee of IEM for assistance during SEM, EDX and XRD measurements.

REFERENCES

1. C.-Y. Chiu, H. Wu, Z. Yao, F. Zhou, H. Zhang, V. Ozolins and Y. Huang, *J. Am. Chem. Soc.*, 2013, **135**, 15489-15500.
2. Y. Xia, Y. Xiong, B. Lim and S. E. Skrabalak, *Angew. Chem. Int. Ed.*, 2009, **48**, 60-103.

3. N. Liu, K. Wang, Y. Gao, D. Li, W. Lin and C. Li, *Colloids Surf., A*, 2017, **535**, 251-256.
4. G. Song, F. Zhou, C. Xu and B. Li, *Analyst*, 2016, **141**, 1257-1265.
5. M. S. Akhtar, J. Panwar and Y.-S. Yun, *ACS Sustainable Chem. Eng.*, 2013, **1**, 591-602.
6. K. P. Adolph, *Journal*, 1928, US Patent, US1663201A.
7. W. F. Von Oettingen and Y. Ishikawa, *J. Am. Pharm. Assoc. (1912-1977)*, 1928, **17**, 124-134.
8. D. Ma, J. Zhao, Y. Zhao, X. Hao, L. Li, L. Zhang, Y. Lu and C. Yu, *Colloids Surf., A*, 2012, **395**, 276-283.
9. R. Abargues, S. Albert, J. L. Valdés, K. Abderrafi and J. P. Martínez-Pastor, *J. Mater. Chem.*, 2012, **22**, 22204-22211.
10. G.-R. Li, F.-L. Zheng and Y.-X. Tong, *Cryst. Growth Des.*, 2008, **8**, 1226-1232.
11. J. Ota and S. K. Srivastava, *J. Phys. Chem. C*, 2007, **111**, 12260-12264.
12. G. E. Smith, G. A. Baraff and J. M. Rowell, *Phys. Rev.*, 1964, **135**, A1118-A1124.
13. V. S. Édel'man, *Soviet Physics Uspekhi*, 1977, **20**, 819-835.
14. E. N. Griбанov, O. I. Markov and Y. V. Khripunov, *Nanotechnologies in Russia*, 2011, **6**, 593.
15. R. He, D. Xu, B. Cheng, J. Yu and W. Ho, *Nanoscale Horiz.*, 2018, **3**, 464-504.
16. K. Mase, M. Yoneda, Y. Yamada and S. Fukuzumi, *ACS Energy Lett.*, 2016, **1**, 913-919.
17. L. Li, C. Tang, B. Xia, H. Jin, Y. Zheng and S.-Z. Qiao, *ACS Catal.*, 2019, **9**, 2902-2908.
18. C. W. Lee, J. S. Hong, K. D. Yang, K. Jin, J. H. Lee, H.-Y. Ahn, H. Seo, N.-E. Sung and K. T. Nam, *ACS Catal.*, 2018, **8**, 931-937.
19. Y. Qiu, J. Du, C. Dai, W. Dong and C. Tao, *J. Electrochem. Soc.*, 2018, **165**, H594-H600.
20. S. Bera, S. Ghosh, S. Shyamal, C. Bhattacharya and R. N. Basu, *Solar Energy Materials and Solar Cells*, 2019, **194**, 195-206.
21. S. Bera, S. Ghosh and R. N. Basu, *New J. Chem.*, 2018, **42**, 541-554.
22. S. Solmi, C. Morreale, F. Ospitali, S. Agnoli and F. Cavani, *ChemCatChem*, 2017, **9**, 2797-2806.
23. Y. Kwon, Y. Birdja, I. Spanos, P. Rodriguez and M. T. M. Koper, *ACS Catal.*, 2012, **2**, 759-764.
24. S. Shafafi, A. Habibi-Yangjeh, S. Feizpoor, S. Ghosh and T. Maiyalagan, *Sep. Purif. Technol.*, 2020, **250**, 117179.

25. E. Vesali-Kermani, A. Habibi-Yangjeh, H. Diarmand-Khalilabad and S. Ghosh, *J. Colloid Int. Sci.*, 2020, **563**, 81-91.
26. M. Gich, C. Fernandez-Sanchez, L. C. Cotet, P. Niu and A. Roig, *J. Mater. Chem. A*, 2013, **1**, 11410-11418.
27. N. M. Shinde, Q. X. Xia, J. M. Yun, R. S. Mane and K. H. Kim, *ACS Appl. Mater. Interfaces.*, 2018, **10**, 11037-11047.
28. N. M. Shinde, Q. X. Xia, J. M. Yun, P. V. Shinde, S. M. Shaikh, R. K. Sahoo, S. Mathur, R. S. Mane and K. H. Kim, *Electrochim. Acta*, 2019, **296**, 308-316.
29. H. Xu, X. Hu, H. Yang, Y. Sun, C. Hu and Y. Huang, *Adv. Energy Mater.*, 2015, **5**, 1401882.
30. L. Li, X. Zhang, Z. Zhang, M. Zhang, L. Cong, Y. Pan and S. Lin, *J. Mater. Chem. A*, 2016, **4**, 16635-16644.
31. H. Yu, P. C. Gibbons and W. E. Buhro, *J. Mater. Chem.*, 2004, **14**, 595-602.
32. Q. Zhang, M. Zhou, G. Ren, Y. Li, Y. Li and X. Du, *Nat. Commun.*, 2020, **11**, 1731.
33. D. San Roman, D. Krishnamurthy, R. Garg, H. Hafiz, M. Lamparski, N. T. Nuhfer, V. Meunier, V. Viswanathan and T. Cohen-Karni, *ACS Catal.*, 2020, **10**, 1993-2008.
34. E. Jung, H. Shin, W. Hooch Antink, Y.-E. Sung and T. Hyeon, *ACS Energy Lett.*, 2020, **5**, 1881-1892.
35. C. Xia, Y. Xia, P. Zhu, L. Fan and H. Wang, *Science*, 2019, **366**, 226-231.
36. S. Yang, A. Verdaguer-Casadevall, L. Arnarson, L. Silvioli, V. Čolić, R. Frydendal, J. Rossmeisl, I. Chorkendorff and I. E. L. Stephens, *ACS Catal.*, 2018, **8**, 4064-4081.
37. S. Siahrostami, A. Verdaguer-Casadevall, M. Karamad, D. Deiana, P. Malacrida, B. Wickman, M. Escudero-Escribano, E. A. Paoli, R. Frydendal, T. W. Hansen, I. Chorkendorff, I. E. L. Stephens and J. Rossmeisl, *Nat. Mater.*, 2013, **12**, 1137-1143.
38. J. M. Campos-Martin, G. Blanco-Brieva and J. L. G. Fierro, *Angew. Chem. Int. Ed.*, 2006, **45**, 6962-6984.
39. Y. Sun, I. Sinev, W. Ju, A. Bergmann, S. Dresch, S. Köhl, C. Spöri, H. Schmies, H. Wang, D. Bernsmeier, B. Paul, R. Schmack, R. Kraehnert, B. Roldan Cuenya and P. Strasser, *ACS Catal.*, 2018, **8**, 2844-2856.
40. J. Lim and M. R. Hoffmann, *Chem. Eng. J.*, 2019, **374**, 958-964.

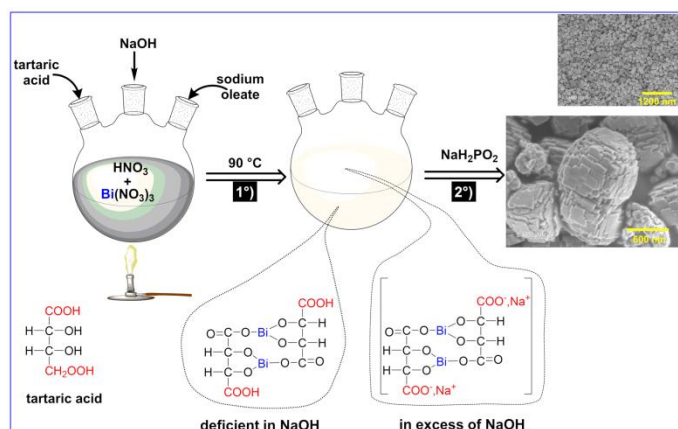
41. Y. Pang, K. Wang, H. Xie, Y. Sun, M.-M. Titirici and G.-L. Chai, *ACS Catal.*, 2020, **10**, 7434-7442.
42. J. H. Baek, T. M. Gill, H. Abroshan, S. Park, X. Shi, J. Nørskov, H. S. Jung, S. Siahrostami and X. Zheng, *ACS Energy Lett.*, 2019, **4**, 720-728.
43. Y. Holade, N. Sahin, K. Servat, T. Napporn and K. Kokoh, *Catalysts*, 2015, **5**, 310-348.
44. G. J. K. Acres, J. C. Frost, G. A. Hards, R. J. Potter, T. R. Ralph, D. Thompsett, G. T. Burstein and G. J. Hutchings, *Catal. Today*, 1997, **38**, 393-400.
45. G.-L. Chai, M. Boero, Z. Hou, K. Terakura and W. Cheng, *ACS Catal.*, 2017, **7**, 7908-7916.
46. P. Su, M. Zhou, X. Lu, W. Yang, G. Ren and J. Cai, *Appl. Catal. B: Env.*, 2019, **245**, 583-595.
47. P. Liang, M. Rivallin, S. Cerneaux, S. Lacour, E. Petit and M. Cretin, *J. Membrane Sci.*, 2016, **510**, 182-190.
48. T. X. H. Le, R. Esmilaire, M. Drobek, M. Bechelany, C. Vallicari, D.-L. Nguyen, A. Julbe, S. Tingry and M. Cretin, *J. Mater. Chem. A*, 2016, **4**, 17686-17693.
49. D. Li, T. Zheng, Y. Liu, D. Hou, H. He, H. Song, J. Zhang, S. Tian, W. Zhang, L. Wang and J. Ma, *Chem. Eng. J.*, 2020, **394**, 125033.
50. T. W. Napporn, Y. Holade, B. Kokoh, S. Mitsushima, K. Mayer, B. Eichberger and V. Hacker, in *Fuel Cells and Hydrogen: From Fundamentals to Applied Research*, eds. V. Hacker and S. Mitsushima, Elsevier, 2018, DOI: 10.1016/B978-0-12-811459-9.00009-8, pp. 175-214.
51. K. Shinozaki, J. W. Zack, S. Pylypenko, B. S. Pivovar and S. S. Kocha, *J. Electrochem. Soc.*, 2015, **162**, F1384-F1396.
52. Y. Garsany, I. L. Singer and K. E. Swider-Lyons, *J. Electroanal. Chem.*, 2011, **662**, 396-406.
53. R. C. M. Jakobs, L. J. J. Janssen and E. Barendrecht, *Electrochim. Acta*, 1985, **30**, 1085-1091.
54. F. T. A. Vork and E. Barendrecht, *Electrochim. Acta*, 1990, **35**, 135-139.
55. N. Elgrishi, K. J. Rountree, B. D. McCarthy, E. S. Rountree, T. T. Eisenhart and J. L. Dempsey, *J. Chem. Educ.*, 2017, **95**, 197-206.

56. W. E. Kosimaningrum, T. X. H. Le, Y. Holade, M. Bechelany, S. Tingry, B. Buchari, I. Noviandri, C. Innocent and M. Cretin, *ACS Appl. Mater. Interfaces.*, 2017, **9**, 22476-22489.
57. B. D. Patterson, E. A. MacRae and I. B. Ferguson, *Anal. Biochem.*, 1984, **139**, 487-492.
58. P. Bonét-Maury, *Compt. rend.*, 218, 117 (1944, *Compt. rend.*, 1944, **218**, 117-119.
59. E. E. Foos, R. M. Stroud, A. D. Berry, A. W. Snow and J. P. Armistead, *J. Am. Chem. Soc.*, 2000, **122**, 7114-7115.
60. J. Fang, K. L. Stokes, W. L. Zhou, W. Wang and J. Lin, *Chem. Commun.*, 2001, DOI: 10.1039/B106105B, 1872-1873.
61. Y. Wang, J. Chen, L. Chen, Y.-B. Chen and L.-M. Wu, *Cryst. Growth Des.*, 2010, **10**, 1578-1584.
62. A. Zalineeva, A. Serov, M. Padilla, U. Martinez, K. Artyushkova, S. Baranton, C. Coutanceau and P. B. Atanassov, *J. Am. Chem. Soc.*, 2014, **136**, 3937-3945.
63. B. Oprea, T. Radu and S. Simon, *J. Non-Cryst. Solids*, 2013, **379**, 35-39.
64. I. G. Casella and M. Contursi, *Electrochim. Acta*, 2006, **52**, 649-657.
65. X. Li, Y. Sun, T. Xiong, G. Jiang, Y. Zhang, Z. Wu and F. Dong, *J. Catal.*, 2017, **352**, 102-112.
66. K. Yin, Z. D. Cui, X. J. Yang, S. L. Zhu, Z. Y. Li and Y. Q. Liang, *J. Electrochem. Soc.*, 2015, **162**, H785-H791.
67. R. M. Arán-Ais, F. J. Vidal-Iglesias, J. Solla-Gullón, E. Herrero and J. M. Feliu, *Electroanalysis*, 2015, **27**, 945-956.
68. H. Yang, Y. Tang and S. Zou, *Electrochem. Commun.*, 2014, **38**, 134-137.
69. S. Hebié, L. Cornu, T. W. Napporn, J. Rousseau and B. K. Kokoh, *J. Phys. Chem. C*, 2013, **117**, 9872-9880.
70. V. Vivier, A. Régis, G. Sagon, J. Y. Nedelec, L. T. Yu and C. Cachet-Vivier, *Electrochim. Acta*, 2001, **46**, 907-914.
71. J. Sun, J. Wang, Z. Li, Z. Yang and S. Yang, *RSC Adv.*, 2015, **5**, 51773-51778.
72. K. Z. Brainina, N. F. Zakharchuk, D. P. Synkova and I. G. Yudelevich, *J. Electroanal. Chem. Interf. Electrochem.*, 1972, **35**, 165-176.
73. V. Vivier, C. Cachet-Vivier, S. Mezaille, B. L. Wu, C. S. Cha, J. Y. Nedelec, M. Fedoroff, D. Michel and L. T. Yu, *J. Electrochem. Soc.*, 2000, **147**, 4252.

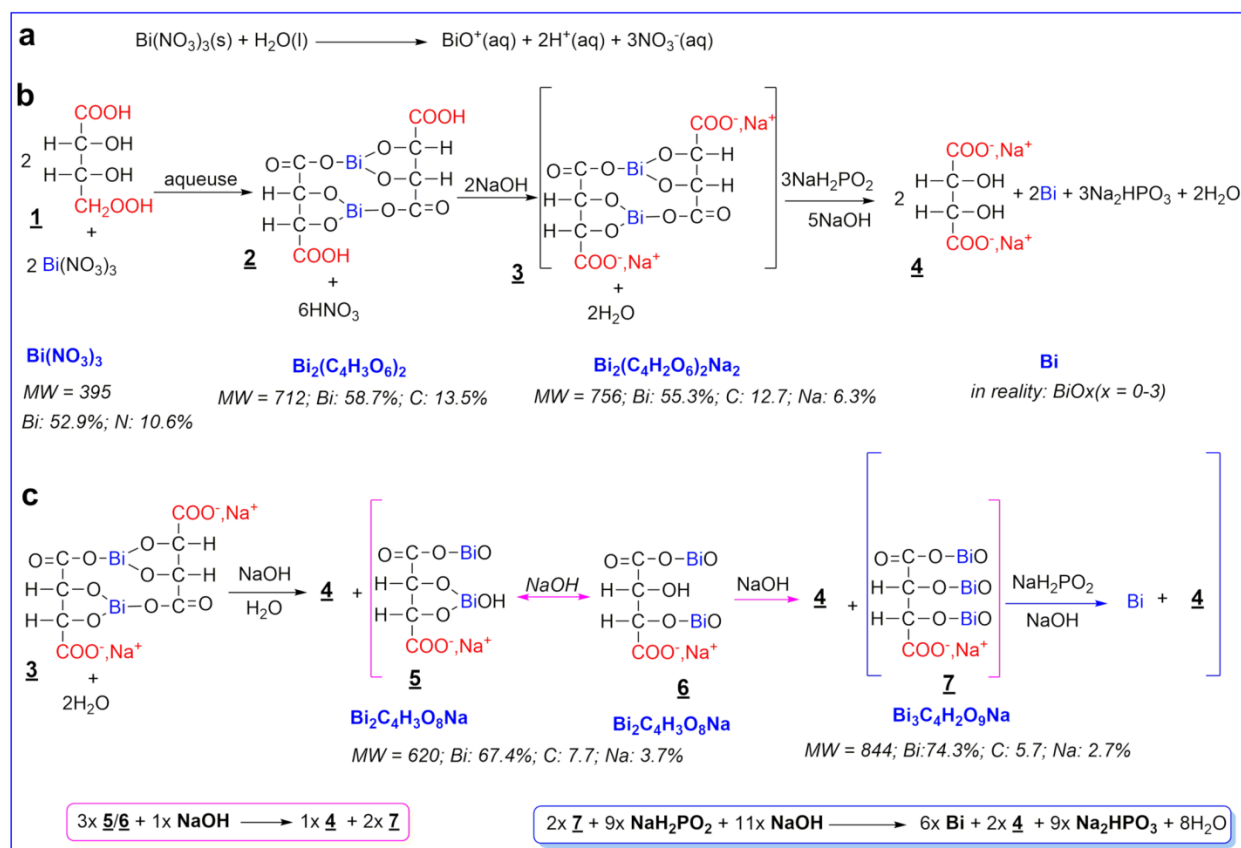
74. X. Huang, J. Yan, F. Zeng, X. Yuan, W. Zou and D. Yuan, *Mater. Lett.*, 2013, **90**, 90-92.
75. F.-L. Zheng, G.-R. Li, Y.-N. Ou, Z.-L. Wang, C.-Y. Su and Y.-X. Tong, *Chem. Commun.*, 2010, **46**, 5021-5023.
76. H.-W. Wang, Z.-A. Hu, Y.-Q. Chang, Y.-L. Chen, Z.-Q. Lei, Z.-Y. Zhang and Y.-Y. Yang, *Electrochim. Acta*, 2010, **55**, 8974-8980.
77. T. P. Gujar, V. R. Shinde, C. D. Lokhande and S.-H. Han, *J. Power Sources*, 2006, **161**, 1479-1485.
78. P. Urchaga, S. Baranton, T. Napporn and C. Coutanceau, *Electrocatalysis*, 2010, **1**, 3-6.
79. Q. Chang, P. Zhang, A. H. B. Mostaghimi, X. Zhao, S. R. Denny, J. H. Lee, H. Gao, Y. Zhang, H. L. Xin, S. Siahrostami, J. G. Chen and Z. Chen, *Nat. Commun.*, 2020, **11**, 2178.
80. M. Ledendecker, E. Pizzutilo, G. Malta, G. V. Fortunato, K. J. J. Mayrhofer, G. J. Hutchings and S. J. Freakley, *ACS Catal.*, 2020, **10**, 5928-5938.
81. M. B. Zakaria, C. Li, M. Pramanik, Y. Tsujimoto, M. Hu, V. Malgras, S. Tominaka and Y. Yamauchi, *J. Mater. Chem. A*, 2016, **4**, 9266-9274.
82. H. W. Kim, M. B. Ross, N. Kornienko, L. Zhang, J. Guo, P. Yang and B. D. McCloskey, *Nat. Catal.*, 2018, **1**, 282-290.
83. A. Lasia, *Electrochemical Impedance Spectroscopy and its Applications*, Springer-Verlag, New York, NY, USA, 2014.
84. M. E. Orazem and B. Tribollet, *Electrochemical Impedance Spectroscopy*, John Wiley & Sons, Inc. , Hoboken, New Jersey, USA, 2 edn., 2017.
85. J. Staszak-Jirkovský, R. Subbaraman, D. Strmcnik, K. L. Harrison, C. E. Diesendruck, R. Assary, O. Frank, L. Kober, G. K. H. Wiberg, B. Genorio, J. G. Connell, P. P. Lopes, V. R. Stamenkovic, L. Curtiss, J. S. Moore, K. R. Zavadil and N. M. Markovic, *ACS Catal.*, 2015, **5**, 6600-6607.

Table 1. Results at 0.6 V vs RHE from RRDE measurement and bulk electrolysis in 1 M KOH.

Entry	RRDE(1600 rpm)			Electrolysis and UV-Vis Assays	
	$\text{HO}_2^{-1}(\%)$	n_{ex}	$j_k(\text{A g}^{-1})$	$\text{HO}_2^{-1}(\text{mol kg}^{-1} \text{ cm}^{-2})$	FE(%)
R30	95.5	2.1	30	69 ± 3	92 ± 4
R12	90.2	2.2	29	44 ± 3	62 ± 5
CP	-	-	-	38 ± 4	37 ± 3



Scheme 1. Illustration of the used strategy to produce a library of bismuth-based materials by regulating the coordination between tartaric acid and bismuth (III).



Scheme 2. Sketch illustrating the synthesis of bismuth-based materials that involves: (a) dissolution of the precursor in nitric acid solution, (b, c) formation of the materials following the reduction of the different complexes of Bi(+III). Note: MW: referred to as molecular weight.

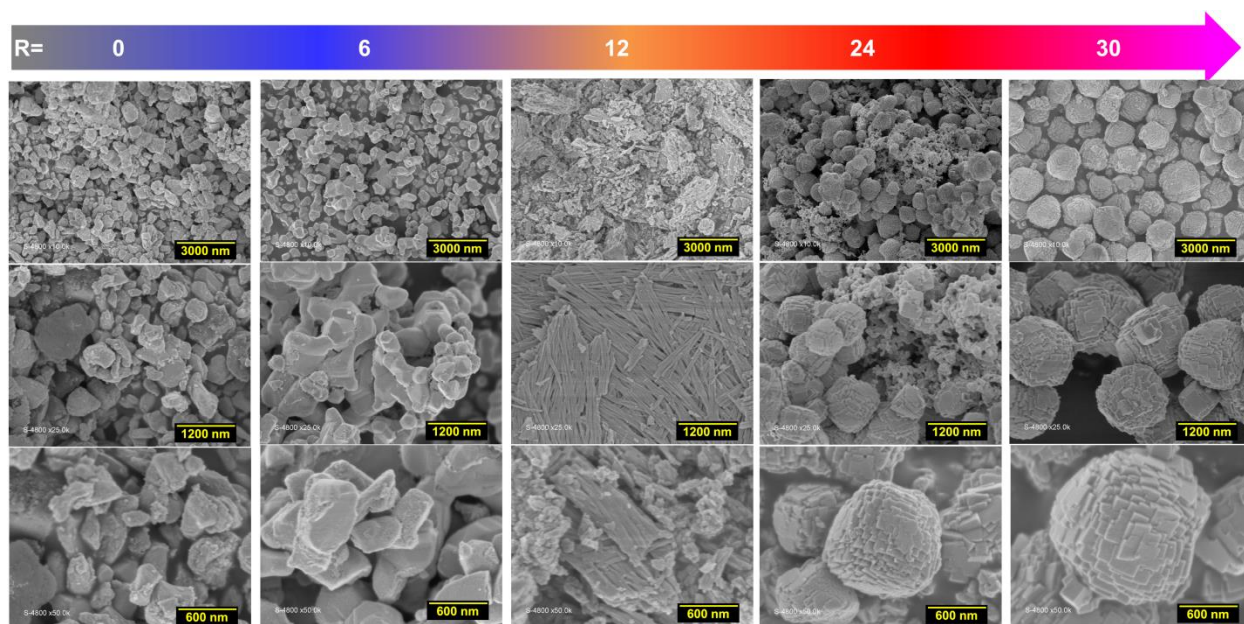


Fig. 1. SEM characterization of the as-synthesized bismuth-based materials at different molar ratios: $R = n(\text{NaOH})/n(\text{Bi}(\text{NO}_3)_3 \cdot 5\text{H}_2\text{O})$. Left to right, materials obtained for $R = 0, 6, 12, 24$ and 30. Top to down: from an overview to a closer-view.

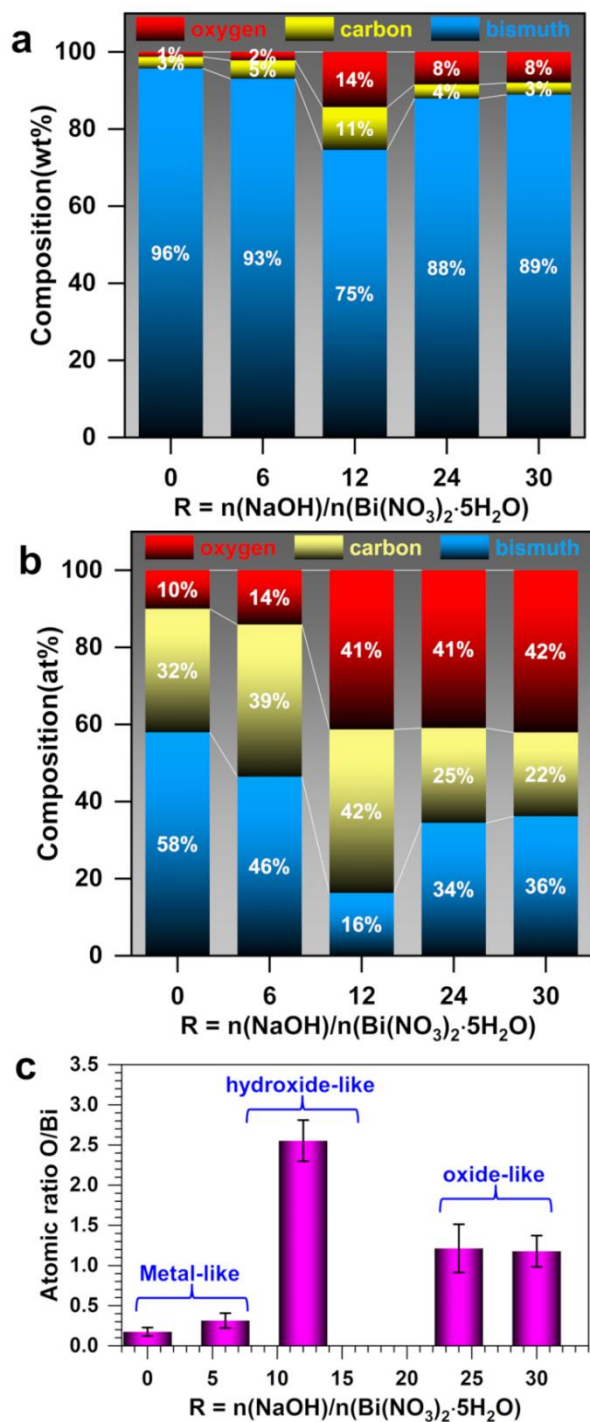


Fig. 2. EDX characterization of the as-synthesized bismuth-based materials at different molar ratios: $R = n(\text{NaOH})/n(\text{Bi}(\text{NO}_3)_3 \cdot 5\text{H}_2\text{O})$. (a) Overall mass composition. (b) Overall atomic composition. (c) Atomic ratio of oxygen/bismuth.

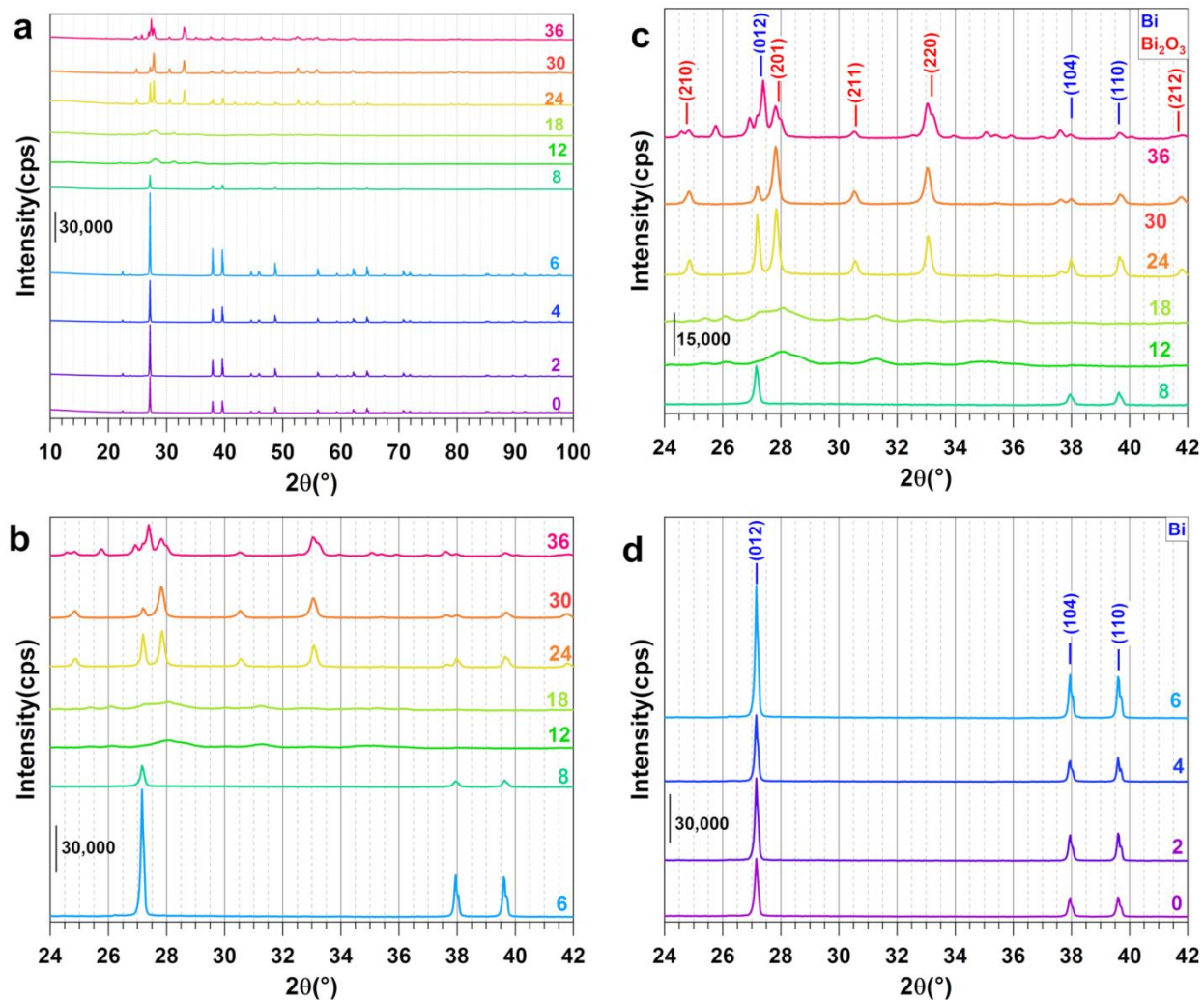


Fig. 3. Powder XRD patterns of the as-synthesized bismuth-based materials at different molar ratios: $R = n(\text{NaOH})/n(\text{Bi}(\text{NO}_3)_3 \cdot 5\text{H}_2\text{O})$. (a, b) Overall comparison of $R = 0$ -36 (a) and $R = 6$ -36 (b). (c, d) Indexed patterns for $R = 8$ -36 (c) and $R = 0$ -6 (d).

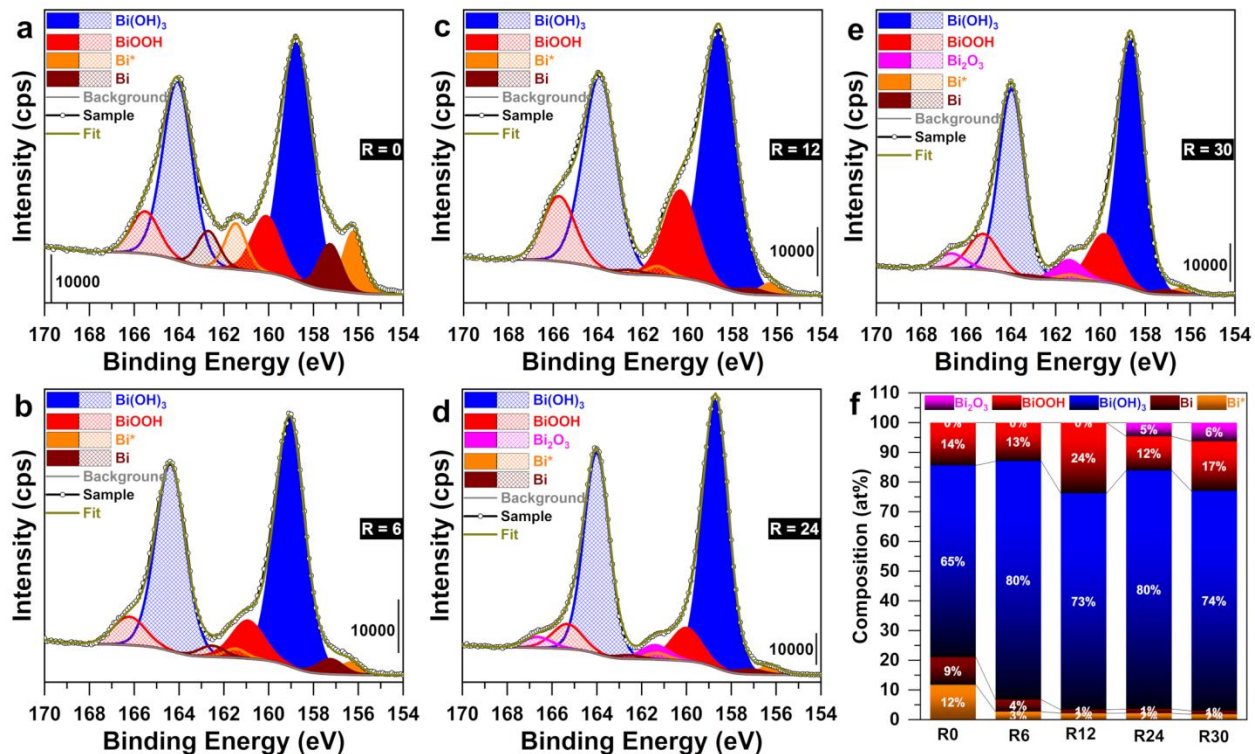


Fig. 4. XPS analysis the as-synthesized bismuth-based materials at different molar ratios: $R = n(\text{NaOH})/n(\text{Bi}(\text{NO}_3)_3 \cdot 5\text{H}_2\text{O})$. (a-e) High-resolution of the Bi 4f region of: (a) $R = 0$, (b) $R = 6$, (c) $R = 12$, (d) $R = 24$, and (e) $R = 30$. (f) Surface atomic composition of bismuth-based species as-determined from XPS.

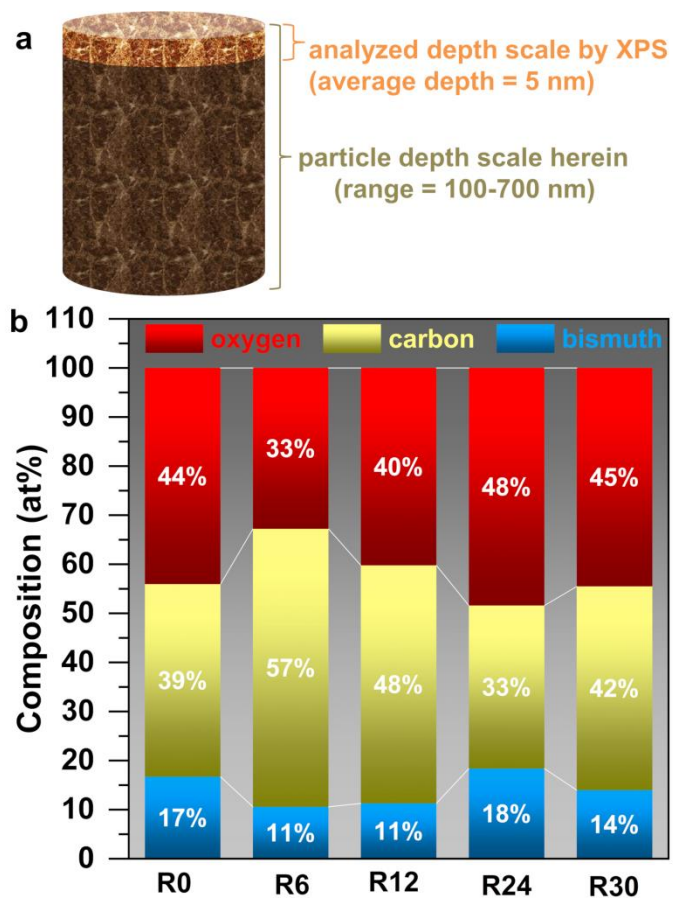


Fig. 5. XPS analysis the as-synthesized bismuth-based materials at different molar ratio: $R = n(\text{NaOH})/n(\text{Bi}(\text{NO}_3)_3 \cdot 5\text{H}_2\text{O})$. (a) Picture showing the portion of the analyzed part by XPS. (b) Overall surface atomic composition of the chemical species as-determined from XPS.

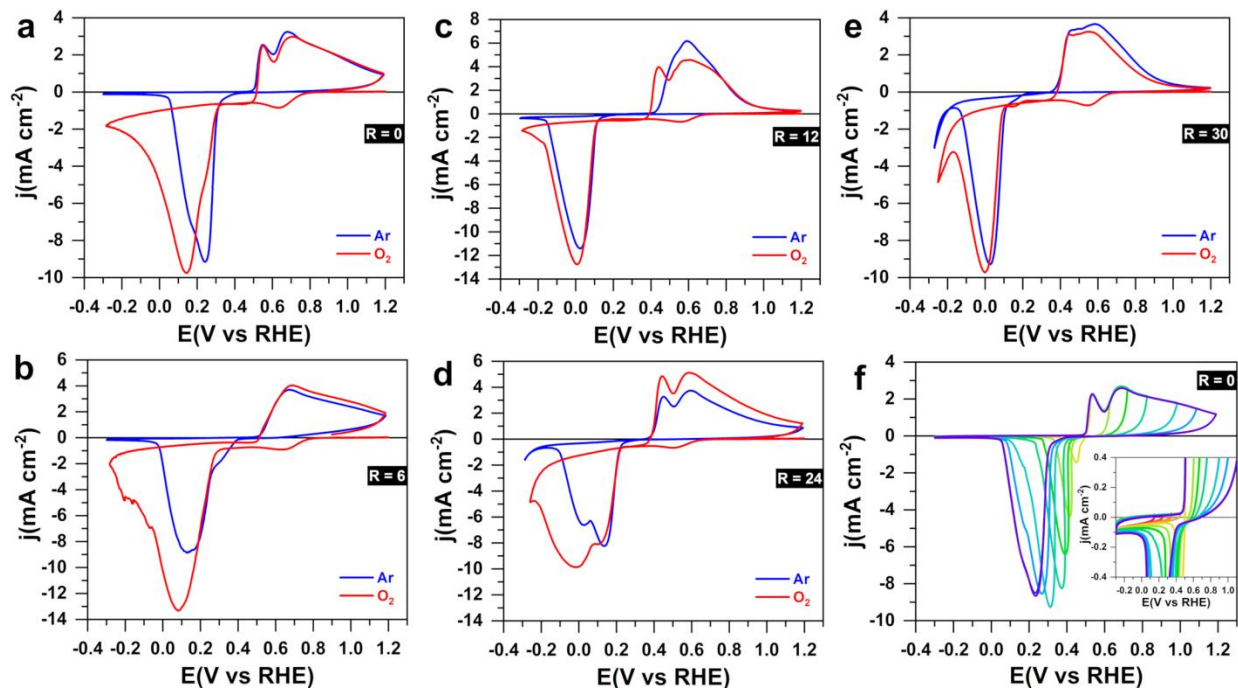


Fig. 6. Characterization by CV of the materials obtained at different molar ratios: $R = n(\text{NaOH})/n(\text{Bi}(\text{NO}_3)_3 \cdot 5\text{H}_2\text{O})$. (a-e) CVs at 100 mV s^{-1} in 0.1 M KOH in the presence of Ar (blue curves, 30th cycle) and in O_2 (red curves: 1st cycle): (a) $R = 0$, (b) $R = 6$, (c) $R = 12$, (d) $R = 24$, and (e) $R = 30$. (f) CVs at 100 mV s^{-1} in Ar-saturated 0.1 M KOH for different upper potential limits for the material obtained for $R = 0$.

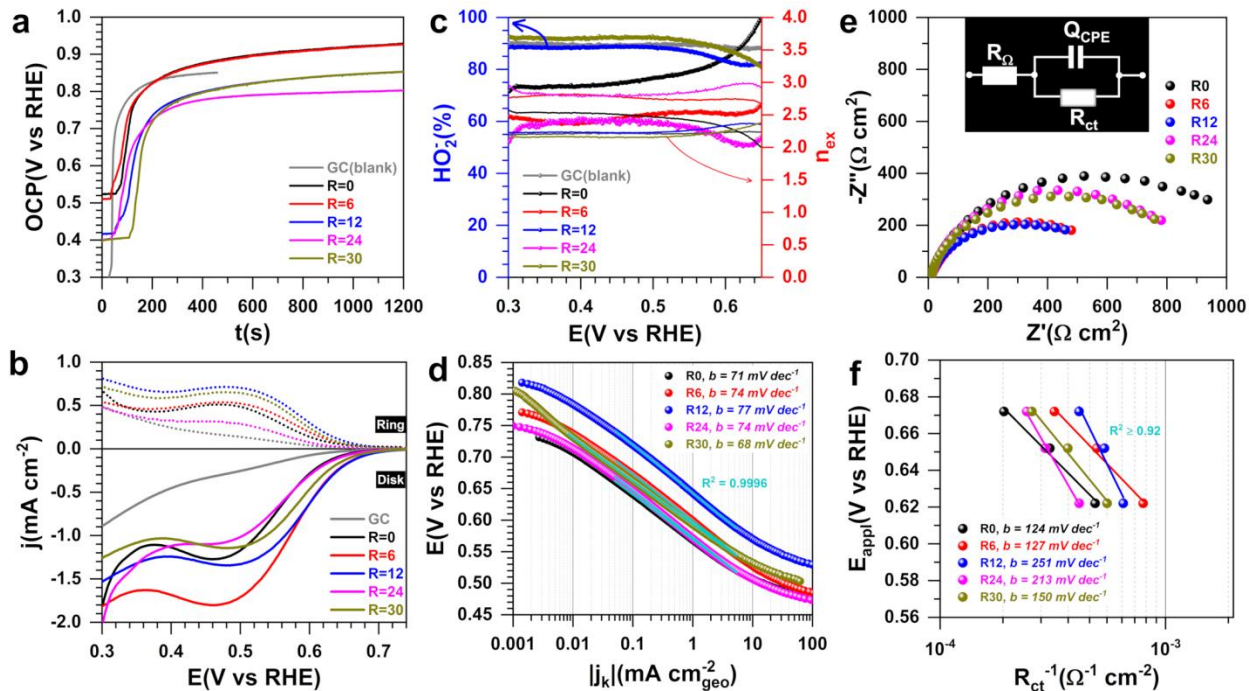


Fig. 7. ORR in 0.1 M KOH for the materials obtained at different molar ratios: $R = n(\text{NaOH})/n(\text{Bi}(\text{NO}_3)_3 \cdot 5\text{H}_2\text{O})$. (a) OCP vs time. (b) LSV curves recorded from a RRDE setup at 5 mV s⁻¹ for the ring (top, normalized by the geometry surface area of the ring (0.11 cm²)) and disk (bottom, normalized by the geometric surface area of the disk (0.196 cm²)): the ring was set at 1.2 V vs RHE. (c) Quantitative results in terms of HO₂⁻ (left y-axis) and transferred number of electrons (right y-axis). (d) Tafel plots by the kinetic current density normalized by the catalyst loading. (e) Complex-plane Nyquist impedance at $E_{\text{appl}} = 0.672$ V vs RHE (inset shows the corresponding electrochemical equivalent circuit of $R_\Omega + Q_{\text{CPE}} // R_{\text{ct}}$). (f) Tafel plots by R_{ct} .

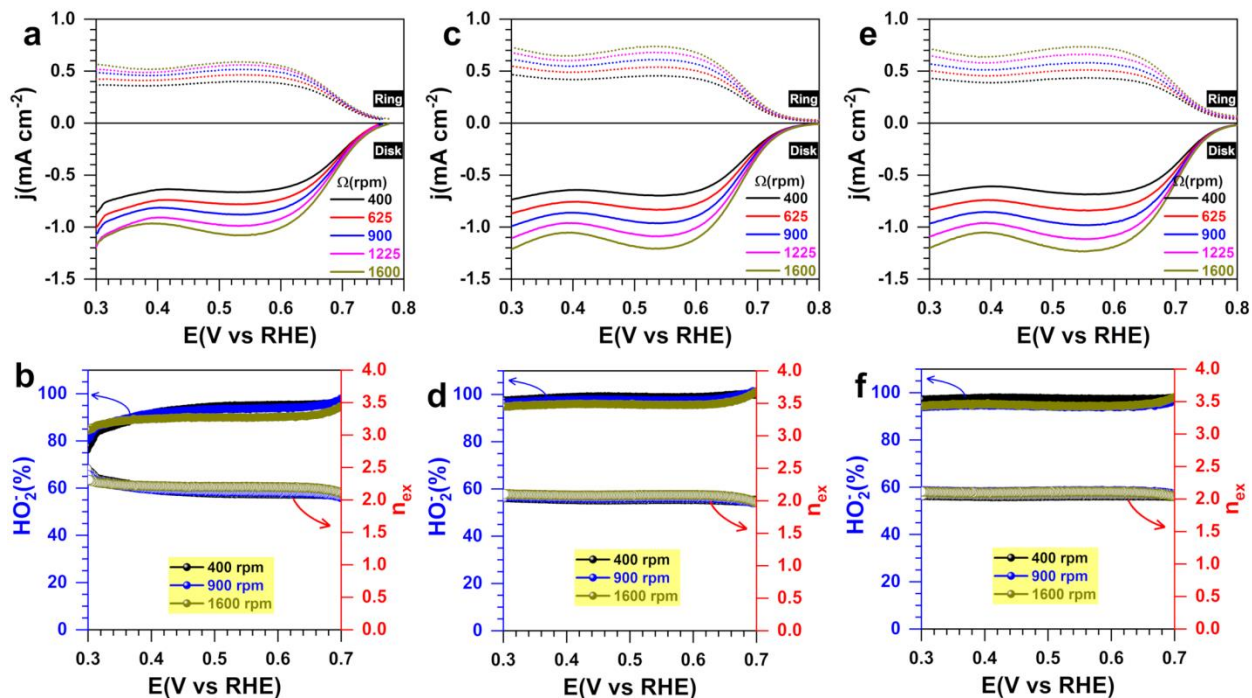


Fig. 8. RRDE measurements during ORR in 1 M KOH for the materials obtained at $R = 12$ (a, b), $R = 30$ (b-f) before AST (a-d) and after AST (e, f). (a, c, e) LSV curves recorded at 5 mV s^{-1} for ring (top, normalized by the geometry surface area of the ring (0.11 cm^2)) and disk (bottom, normalized by the geometric surface area of the disk (0.196 cm^2)): the ring was set at 1.2 V vs RHE . (b, d, f) Quantitative results in terms of HO_2^- (left y-axis) and transferred number of electrons (right y-axis).

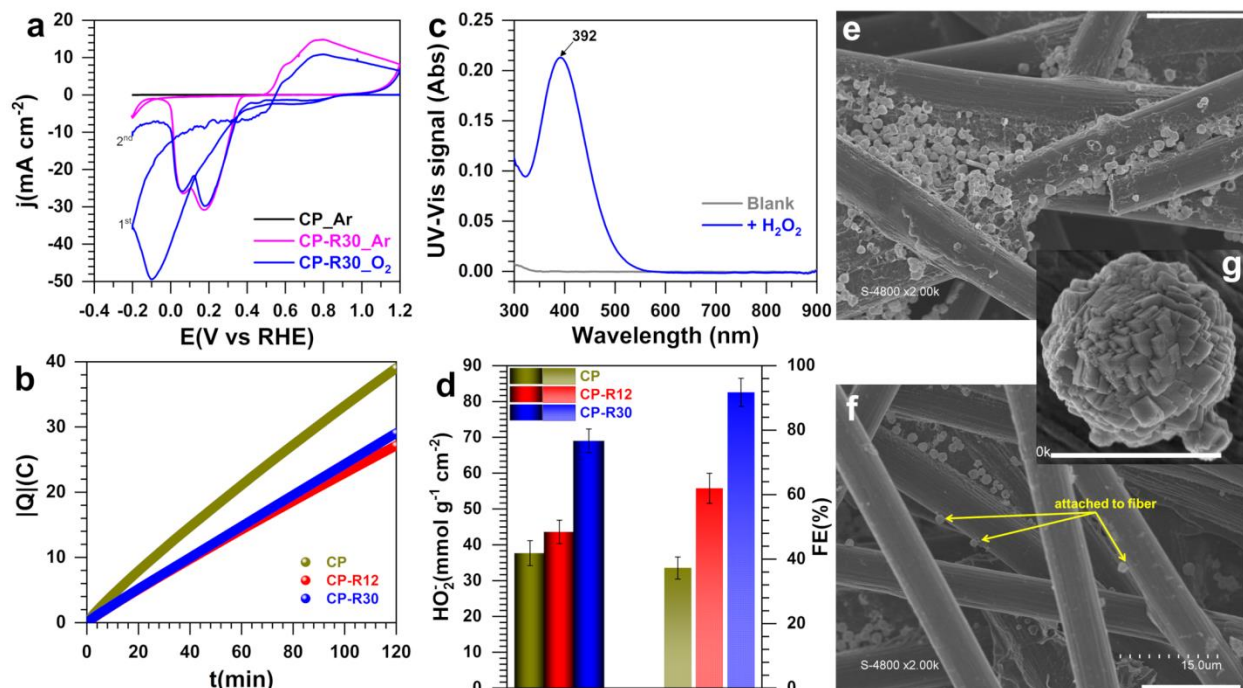


Fig. 9. Bulk electrolysis. (a) Control CVs at 100 mV s⁻¹ in the H-type cell in 1 M KOH for the bare CP electrode and the modified CP electrode by catalytic ink of the material obtained for $R = 30$: in the presence of Ar (30th cycle) and in O₂-saturated electrolyte (1st cycle starting at OCP = 0.98 V vs RHE and 2nd cycle). (b) Electrical charge passed during the potentiostatic electrolysis at an applied potential of 0.6 V vs RHE (iR-uncorrected). (c) UV-Vis spectra of a sulfuric acid + potassium titanium oxalate solution in the absence and presence of the hydrogen peroxide from the electrolysis (after stabilization to pH = 3.5). (d) Quantified hydrogen peroxide by the UV-Vis assays in terms of productivity (left y -axis) and faradaic efficiency (right y -axis). (e-g) Post-mortem SEM and HRSEM images of the CP-R30 electrode after bulk electrolysis: The scale bar = 15 μ m for panels (e, f) and 0.15 μ m for panel (g). Error bars represent 1 SD ($n \geq 3$).